Pseudo-3D techniques for analysis and interpretation of high-resolution marine seismic reflection data

L. Gasperini, M. Ligi and G. Stanghellini

Istituto di Scienze Marine, Consiglio Nazionale delle Ricerche (ISMAR-CNR), Sezione di Bologna, Italy

ABSTRACT   The increasing quality and resolution of marine seismic reflection data, as well as their availability in digital form within large data sets, require the development and testing of new techniques to improve their interpretation. In this work, we present a case study dealing with application of 3D techniques to a set of 2D shallow-water data, where the effect of lateral reflections/diffractions can be neglected. We show how such techniques can be effective in highlighting geological properties/features of the seafloor and sub-seafloor, including reflectivity analysis of prominent horizons, seismic facies classification based on definition of acoustic properties, and compilation of a "flattened" version of seismic sections, by time shifting a particular reflector to a horizontal reference level. This latter technique enables compilations of pseudo-3D grids of seismic volumes, that could be subsequently sampled (time sliced) allowing for compilation of seismic amplitude and reflectivity maps which could be used to infer geological properties and processes.

Key words: marine seismic reflection, pseudo-3D, CHIRP-sonar, reflectivity, seismic facies.

1. Introduction

Natural or artificial shallow-water environments, such as coastal areas, harbours, waterways, lakes, and lagoons, are important economic areas in general affected by anthropogenic pressures. For this reason, they require periodic monitoring, to mitigate environmental crises caused by human activity or natural processes. Being close to modern and/or ancient settlements, they are also important for archeological, paleoanthropological, and paleo-environmental studies, which often find in such environments well preserved and continuous stratigraphic records. On the other hand, the presence of a relatively continuous record could be useful for studying geological processes, such as slip over active faults, mass wasting, and gravitative instability, or other events which may cause natural hazards and could potentially leave characteristic markers in the sedimentary deposits. Another advantage of seismic reflection surveys in submerged environments, compared to their equivalent onshore, is the good coupling between the seismic source and the water (or water saturated) medium, which enhances the quality of acoustic imaging.

Due to several reasons, geophysical studies in shallow-water environments (shallower than a few metres) are not a consolidated practice to date. However, their economic and social importance calls for development of new technologies and methods, which could be offered to a wider range of researchers. Recent progress in the field of marine robotics (remote operating vehicles, autonomous

surface vehicles, etc) provides an interesting opportunity, and opens the door to multidimensional/ multiparametric acquisition and analysis of marine geophysical data (Stanghellini *et al.*, 2020). CHIRP-sonar seismic sources are particularly effective for shallow-water geological studies. In fact, the highly-repeatable frequency-modulated signal generated by these systems leads to an accurate estimate of seafloor reflectivity, and could be used to infer geological properties of the seafloor. Furthermore, taking advantage of the shallow waters and of the consequent closely-spaced survey lines, eventually collected using autonomous vehicles, pseudo-3D techniques could be successfully employed to determine lateral variations of acoustic facies of seismostratigraphic units. All acoustic parameters derived from these data could be used to compile thematic maps, which could include 2D, pseudo-3D, 3D, or 4D (repeated in time) representation of geological properties and processes in any given study area (e.g. Gasperini *et al.*, 2020).

To test the effectiveness of pseudo-3D algorithms for geological interpretation of high resolution marine seismic reflection data, we used a CHIRP-sonar data set (Fig. 1) collected during MARMARA2011 cruise in the Saros Gulf (NE Aegean Sea), along the principal deformation zone of the North Anatolian Fault (NAF).

The Saros Gulf is a triangular-shaped basin between the Gelibolu and the Thrace peninsulas (Fig. 1), widening and deepening towards the west. Since the earliest geological work in the area, its formation has been related to the activity of the NAF system (Gutzwiller, 1921).

Morphobathymetric data suggest that the principal deformation zone of the NAF cuts rectilinearly the gulf in its shallower eastern sector, while broadening towards the deepest sectors towards the west, showing transtensive deformations (Gasperini *et al.*, 2011a). As in other Mediterranean shelves, we assume that sectors shallower than -120 m were exposed subaerially during the Last Glacial Maximum, thus the expected Holocene sediments on the shelf should be a combination of drowned erosional surfaces and shallow-water shoreface
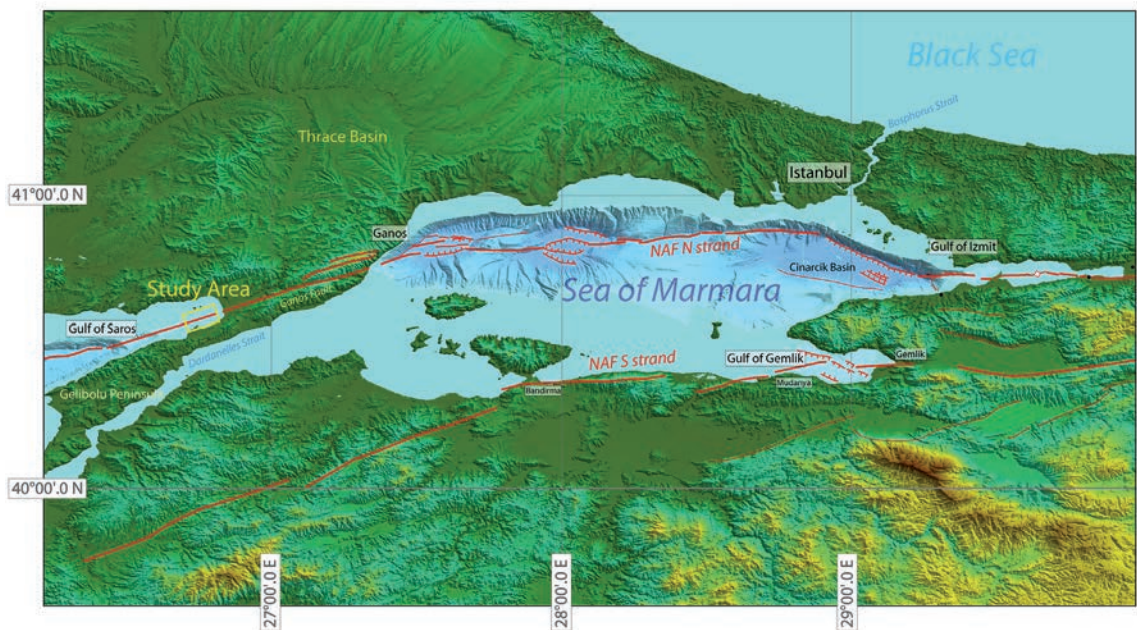

Fig. 1 - Morphostructural map of the NAF system in the Marmara Sea (NW Turkey) modified from Gasperini *et al.* (2011a). The study area along the submerged portion of the Ganos Fault in the Saros Gulf (NE Aegean Sea) is indicated by the yellow box.

sediments, overlapped by fine grained marine sediments deposited after the latest transgression (Gasperini *et al.*, 2011a). Because the NAF is an active fault system, these deposits should be affected by tectonic activity, which could include strike-slip, transtensional, and transpressional deformations, that can be detected in our data set. In 2011, a densely-spaced grid of high resolution seismic profiles was collected in this region onboard of R/V Urania, between 5 and 100 m of water depth (Gasperini *et al.*, 2011b). Here, we present innovative pseudo-3D data processing to highlight the shallow geological feature of this complex area.

2. Methods

2.1. Data processing

The seismic reflection profiles analysed in this work were collected using a 15 transducer, Bentos CHIRP III system. They have the following characteristics: i) a highly-repeatable frequency-modulated signal generated by the seismic source; ii) a constant emission power and receiver gain; iii) a densely-spaced, regular grid of acquisition.

Data were processed using SeisPrho (Gasperini and Stanghellini, 2009), applying static corrections, gain normalisation, spherical divergence correction, and band-pass filtering, as well as pseudo 3D algorithms that will be described below. CHIRP technology uses digital linear frequency modulated (FM) acoustic transmissions to produce high-resolution images of the sub-bottom layers (Fig. 2). The first sweep signal processing step is to cross-correlate the transmitted signal with the received signal (Schock *et al.*, 1989; Dal Forno and Gasperini, 2008). In this way, the long outgoing sweep signal is compressed, and the resulting wavelet is similar to the conventional seismic signal.

### 2.2. Reflectivity analysis and vertical resolution

The cross-correlation step is usually carried out by the acquisition system, as it requires exact knowledge of the generated output signal. The Bentos CHIRP III system generates a 0.02 s (T) long signal $w(t)$ modulated in amplitude and frequency with a linearly variable frequency from 2 (f_{min}) to 7 (f_{max}) kHz (Fig. 2) based on the following formula:

$$w(t) = \begin{cases} A(t)\cos[2\pi(f_0 + kt)t] & \forall t \in \left[-\dfrac{T}{2}, \dfrac{T}{2}\right] \\ 0 & elsewhere \end{cases} \tag{1}$$

where $A(t)$ is the Blackmann-Harris envelope function (Harris, 1978) that defines variations of the signal amplitude with time, $f_0 = (f_{min} + f_{max})/2$ is the bandwidth mid-frequency, and $k = (f_{max} - f_{min})/T$ is the change rate of frequency with time. The waveform generated by the Bentos CHIRP III system are property of the manufacturer and, therefore, parameters for $A(t)$ are not known by the end user.

The autocorrelation function of the output signal, generated by the system (Fig. 2a), gives as a result a zero-phase signal called Klauder wavelet (Fig. 2b) and represents the compressed source wavelet $w_k(t)$. In the absence of environmental noise and changes in the waveform of the output signal due to inelastic losses along its ray path, the recorded signal results from the convolution

Fig. 2 - CHIRP pulse: a) example of the transmitted source wavelet. The Blackmann-Harris envelope function used to scale amplitude with time in Eq. 1 is $A(t) = 0.359 + 0.488 \cos(2\pi t/T) + 0.141 \cos(4\pi t/T) + 0.012 \cos(6\pi t/T)$; b) autocorrelation function of source wavelet shown in panel a. The autocorrelation of a CHIRP pulse is a zero-phase Klauder wavelet.
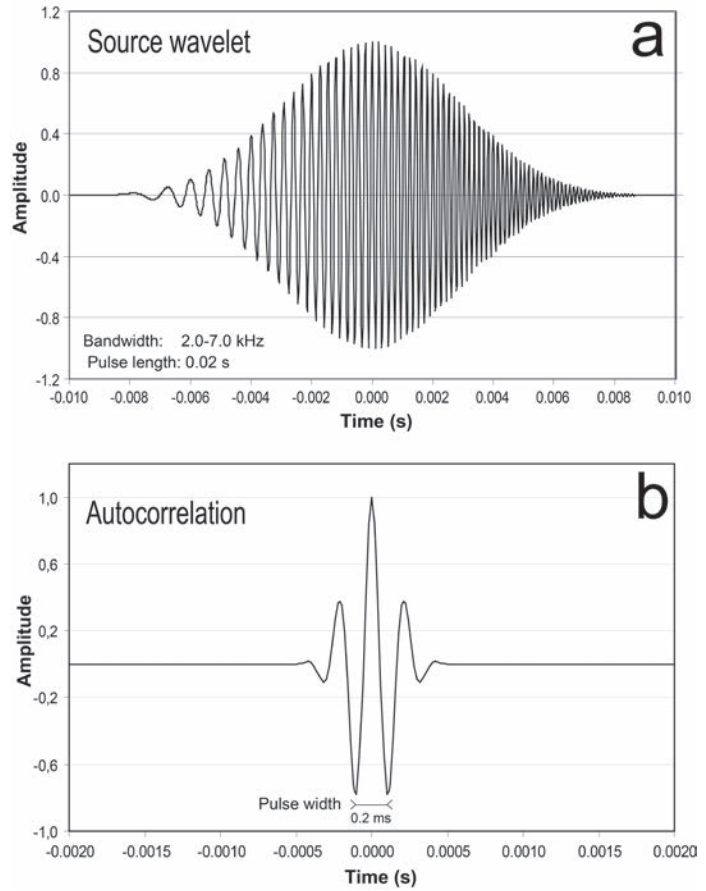
between the compressed source signal $w_k(t)$ and the earth reflectivity $e(t)$. The return signal is sampled by the system at a frequency of 32 kHz allowing a Nyquist frequency of 16 kHz, much higher than the maximum frequency content of the generated output signal (7 kHz). This technique avoids the use of analogic anti-alias filters before sampling. In our forward modelling, synthetic seismograms are obtained assuming that the de-chirped pulse (or the compressed wavelet) of the system is a Klauder wavelet with the form (Fig. 3a):

$$w_k(t) = \Re e\left\{ A \frac{\sin[\pi k(T-t)t]}{\pi k t} \exp(2\pi i f_0 t) \right\} \qquad \forall t \in \left[-\frac{T}{2}, \frac{T}{2} \right] \qquad (2)$$

where A is a constant and $i^2 = -1$.

The ability to distinguish closely spaced reflectors defines the vertical resolution in seismic reflection profiles. For an impulsive source, the wavelength of the generated signal determines the vertical resolution of the system ($\lambda/4$), while, in a multi-frequency system such as a CHIRP-sonar, it depends from the bandwidth of the transmitted pulse. In the latter case, taking into account the two-way travel time, the theoretical vertical resolution is defined by the half-product between the width of the central peak of the compressed pulse and the wave velocity in the medium (Fig. 3b):

Resolution limit = Pulse width × Sound velocity / 2
where the Pulse width = 1 / Bandwidth.   (3)

Hence, the vertical resolution of a CHIRP III system, with frequencies between 2 and 7 kHz (centred around 5 kHz), is 0.0001 s, that corresponds to a distance of 0.154 m assuming an average P wave velocity of about 1,540 m/s in soft sediments. This is shown in Fig. 3b, where the Klauder wavelet (Fig. 3a) is reflected by two interfaces with reflectivity equal to 1, placed at increasing distances with steps of 0.00002 s. When the two reflectors are located at a distance (in terms of travel time) below the resolution limit of 0.0001 s, the signal reflected by the two reflectors goes into phase construction and the two reflections are indistinguishable, while, for distances greater than the resolution limit, the two resulting reflected echoes are clearly distinguishable (Fig. 3b).

Most CHIRP-sonar systems display and store on disk trace envelopes (reflection strength) of recorded signals losing their phase information. As a consequence, the stored data cannot be processed further, and results cannot be compared directly with those from other single channel seismic systems and/or from forward modelling. Next, we estimate earth reflectivity pattern from stored reflection strength combining source wavelet information with envelope inversion (Ligi *et al.*, 2018).
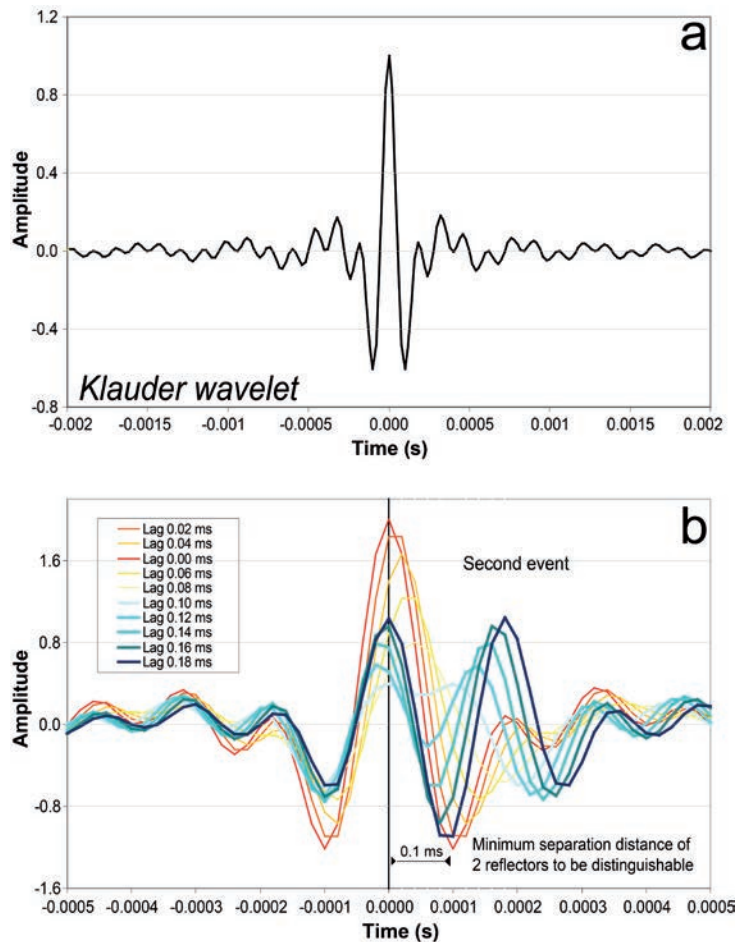

Fig. 3 - a) Klauder wavelet generated using Eq. 2 with A = 1, T = 0.02 s, f_{min} = 2 kHz and f_{max} = 7 kHz. b) Reflected signals from two interfaces at increasing distances with steps of 0.00002 s [~1.54 cm assuming a sound velocity of 1540 m/s, modified from Ligi *et al*. (2018)].

A seismic trace $x(t)$ and its quadrature $y(t)$ may be considered as the real and imaginary part of an analytical signal $z(t)$. The imaginary part $y(t)$ is the Hilbert transform of $x(t)$, i.e. the 90-degree phase-shifted version of the real part (Oppenheim and Schafer, 2010):

$$z(t) = x(t) + i\, y(t) \tag{4}$$

with

$$y(t) = H\{x(t)\} = \frac{1}{\pi t} * x(t) = P\int_{-\infty}^{\infty} \frac{1}{\pi \tau}\, x(t-\tau)d\tau \tag{5}$$

where H is the Hilbert operator, * stands for convolution, and P is the Cauchy principal value.
In polar form $z(t)$ becomes:

$$z(t) = R(t)e^{i\varphi(t)} \quad \text{with } R(t) = \sqrt{x^2(t) + y^2(t)} \text{ and } \varphi(t) = arctg\left[\frac{y(t)}{x(t)}\right] \tag{6}$$

where $R(t)$ represents the instantaneous amplitude (i.e. the signal envelope) and $\varphi(t)$ is the instantaneous phase. The signal envelope $R(t)$ does not retain all the characteristics of the seismic signal $x(t)$ being proportional to the square root of the total energy of the signal at an instant of time. It only provides a measure of the reflection strength of seismic horizons (Fig. 4).
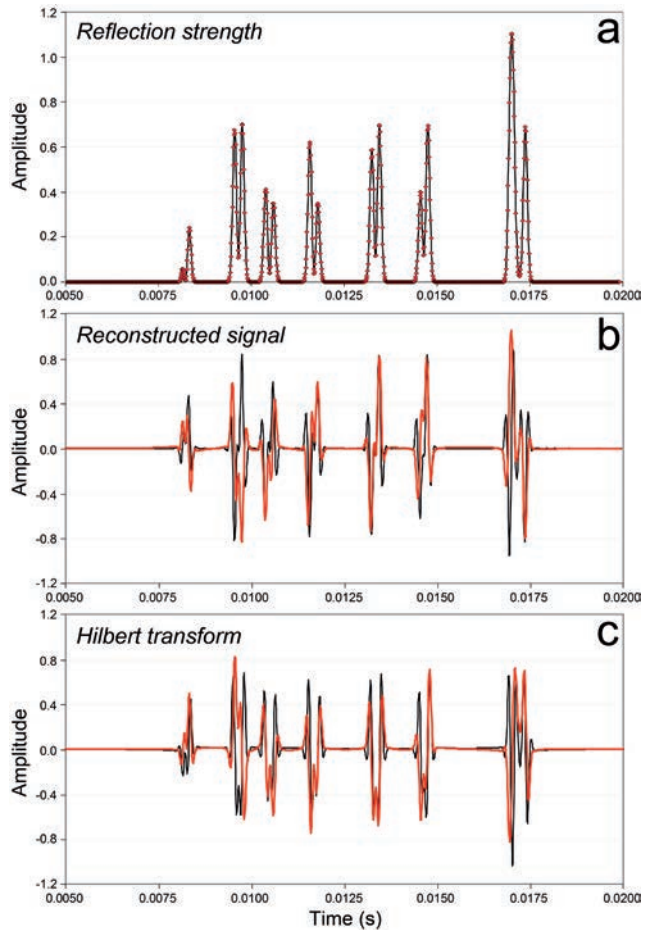

Fig. 4 - Signal envelope and minimum phase reconstructed signal: a) thick red line represents the reflection strength of a synthetic signal obtained convolving the zero-phase source wavelet in Fig. 3a with the earth reflectivity pattern in Fig. 5b. Red diamonds depict the envelope of the reconstructed signal after envelope inversion; b) the real part of the recovered signal (red solid line) is compared with that of the original synthetic signal (black solid line); c) the Hilbert transform (imaginary part) of original (black line) and recovered analytical signal (red line) are compared.

Retrieving a time domain signal from its envelope (similarly from a spectrogram) is a challenging and interesting problem in math and signal processing and has received attention in the past (Voelcker, 1966; Hayes *et al.*, 1980; Kumaresan and Rao, 1999).

A periodic analytical signal $s(t)$ with period T, fundamental frequency $\Omega = 2\pi/T$ and finite bandwidth may be represented by the expression:

$$s(t) = \alpha(t)e^{i\phi(t)} = A_c e^{\ln[\alpha(t)]+iH\{\ln[\alpha(t)]\}}e^{\beta(t)-iH\{\beta(t)\}+\omega_c t} \tag{7}$$

where A_c is the amplitude of the signal, the former exponential corresponds to the minimum-phase component of the complex signal (all the zeros inside the unit circle), while the second exponent constitutes the maximum-phase component (all the zeros outside the unit circle). $\beta(t)$ is a function of $\Phi(t)$; with $w_c = k\Omega$, plus any frequency translation to which the signal $s(t)$ has been subjected (Voelcker, 1966; Kumaresan and Rao, 1999). In order to recover completely $s(t)$, the log-envelope plus the phase of the signal are required. Eq. 7 describes a stationary and periodic model, however true seismic signals are not stationary and certainly non-periodic. Hence, to apply the model of Eq. 7 to seismic traces, we may consider the recorded seismic signal with a length of T seconds as a part of a longer stationary signal extended periodically. This task may be achieved by mirroring the stored envelope $R(t)$ to obtain a periodic signal with period $2T$ and fundamental frequency π/T.

Let us introduce the new function:

$$\widetilde{u}(t) = 2\ln[R(t)] \implies R^2(t) = e^{\widetilde{u}(t)} = e^{2\ln[R(t)]} \tag{8}$$

Adding and subtracting the term $i\varphi(t)$ at the exponent of Eq. 8, we obtain:

$$R^2(t) = e^{\ln[R(t)]+i\varphi(t)}e^{\ln[R(t)]-i\varphi(t)} = z^*(t)\overline{z^*(t)} \tag{9}$$

Let $\varphi(t)$ the Hilbert transform of the log-envelope $u(t) = \ln[R(t)]$, it follows that:

$$z^*(t) = e^{u(t)+iH\{u(t)\}} = e^{\ln[R(t)]+iH\{\ln[R(t)]\}} = e^{u^+(t)} \tag{10}$$

Comparing Eqs. 7 and 10, we deduce that $z^*(t)$ is the minimum-phase component of $z(t)$. The signal envelope $R(t)$ is known and, consequently, also its logarithm, it follows that in order to estimate $z^*(t)$ from Eq. 10, we have to perform the Hilbert transform of $u(t)$. The Hilbert transform of a function can be easily evaluated in the frequency domain by first taking its Fourier transform:

$$U(\omega) = F\{u(t)\} = \int_{-\infty}^{\infty}u(t)e^{-i\omega t}\,dt \tag{11}$$

and then adopting the auxiliary function that vanishes before $\omega = 0$:

$$U^+(\omega) = \begin{cases} 2\,U(\omega) & \forall t > 0 \\ U(\omega) & t = 0 \\ 0 & \forall t < 0 \end{cases} . \tag{12}$$

Taking the inverse Fourier transform of $U^+(\omega)$ to return in the time domain, we obtain the time signal $u^+(t)$:

$$u^+(t) = F^{-1}\{U^+(\omega)\} = \frac{1}{2\pi} \int_{-\infty}^{\infty} U^+(\omega)e^{i\omega t}d\omega . \tag{13}$$

Finally, according to Eq. 10, the estimated minimum-phase component $z^*(t)$ of the analytical signal $z(t)$ can be obtained after exponentiation of $u^+(t)$.

The reconstruction problem of a given target envelope $R(t)$ may be stated as follows: find a signal $z^(t)$ such that $R^(t)-R(t) = 0$. Let us introduce a real positive-valued function $G(z)$ that applies on any signal z with a length of $2T$:

$$G(z) = \sum_t \left(\hat{R}_t - R_t\right)^2 . \tag{14}$$

This function reaches an absolute minimum when the signal $z^(t)$ has the required envelope $R(t)$ suggesting an iterative optimisation approach with the estimated minimum-phase signal $z^*(t)$ as initial guess. The j-th iteration starts by calculating the envelope of the signal estimate $R^_j$. The result is compared to the target R using the objective function G, then the value of G is used to obtain a new estimated signal $z^_{j+1}$. The iteration process is terminated after n iterations when the minimum of G function is found providing the best estimate signal $z^_n(t)$ where the real part $Re[z^_n(t)]$ represents the reconstructed signal $x^(t)$ of $x(t)$. Results of the proposed two step reconstruction procedure are shown in Fig. 5. Assuming noise-free seismic traces, the recorded signal $x(t)$ can be approximated by the convolution product of the source wavelet $w(t)$ with the earth's impulse response $e(t)$ (convolutional model of earth):

$$x(t) = w(t)*e(t) . \tag{15}$$

A recorded CHIRP signal has been simulated by a synthetic trace obtained by convolving the Klauder wavelet in Eq. 2 with the reflectivity pattern $e(t)$ of Fig. 5b; its envelope was, then, calculated (Fig. 4a) being the target envelope in Eq. 14. Figs. 4b and 4c show comparisons between the synthetic signal and the reconstructed signal and its quadrature (Hilbert transform).

The reflectivity pattern $e(t)$ can be inferred by inversion of Eq. 15. Anelastic energy absorption of a source signal penetrating the Earth interior induces minimum-phase and amplitude attenuation of high frequencies. Thus, earth filter $e(t)$ may be assumed to have a minimum phase impulse response. These effects are more significant for a non-impulsive than for an impulsive source. The Klauder wavelet $w_k(t)$ in Eq. 2, resulting from the autocorrelation of the sweep CHIRP signal in Eq. 1, is a zero-phase wavelet. It follows that deconvolution with its inverse produces a
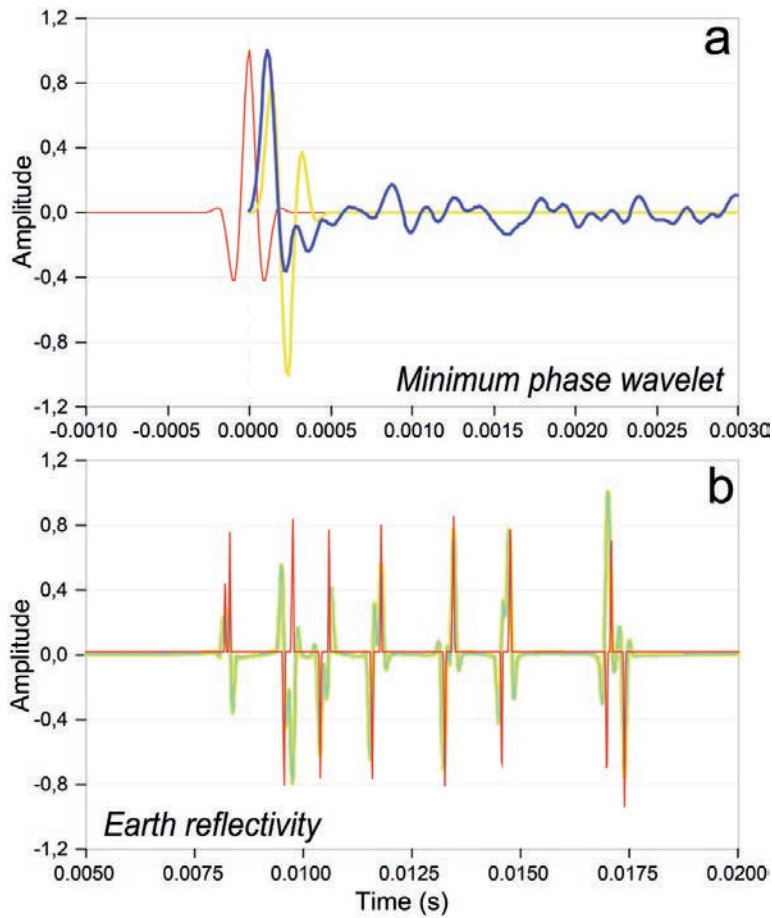
Fig. 5 - Minimum-phase wavelet and earth reflectivity: a) solid yellow line represents the minimum-phase wavelet equivalent to the zero-phase source wavelet (red line), while solid blue line is the minimum-phase wavelet extracted from the reconstructed signal based on the assumption of white reflectivity series; b) earth reflectivity patterns estimated after spiking deconvolution of the reconstructed signal with the inverse of the minimum phase wavelets in panel a are compared with the reflectivity synthetic model (red line). Note that there are no significant differences between the two deconvolved signals (yellow and blue lines).

mixed-phase signal and the earth reflectivity $e(t)$ cannot be recovered properly because spiking deconvolution is based on the minimum-phase assumption. This problem can be overcome designing a filter that convert the Klauder wavelet into its minimum-phase equivalent. This can be implemented in the frequency domain from the autocorrelation function of the Klauder wavelet (Yilmaz, 2001):

$$R_{w_k}(\omega) = W_{w_k}(\omega)\overline{W_{w_k}}(\omega) \quad with \quad W_{w_k}(\omega) = A_{w_k}(\omega)e^{i\phi_{w_k}(\omega)} . \tag{16}$$

Let us define the function:

$$U_w(\omega) = \ln[R_{w_k}(\omega)] \quad \Rightarrow \quad R_{w_k}(\omega) = e^{U_w(\omega)} = e^{\frac{U_w(\omega)}{2}} e^{\frac{U_w(\omega)}{2}} \tag{17}$$

and rewriting Eq. 17 adding and subtracting the term $i\phi_w(\omega)/2$ in the exponents, we obtain:

$$R_{w_k}(\omega) = e^{\frac{1}{2}\left[U_w(\omega)+i\phi_w(\omega)\right]} e^{\frac{1}{2}\left[U_w(\omega)-i\phi_w(\omega)\right]}. \tag{18}$$

When Eq. 18 is compared with Eq. 16, we see that:

$$W_{w_k}(\omega) = e^{\frac{1}{2}\left[U_w(\omega)+i\phi_w(\omega)\right]}. \tag{19}$$

Assuming $W_{w_k}(\omega)$ a minimum-phase signal, $\Phi_w(\omega)$ turns out to be the Hilbert transform of $U_w(\omega)$ (Claerbout, 1985).

Following the method illustrated above, the Hilbert transform can be evaluated first back to the time domain by taking the inverse Fourier transform of $U_w(\omega)$; then double the positive time values, leave the zero-lag alone, and set the negative times to zero to obtain a causal time function $u_w^{+}(t)$.

Then return to the frequency domain to get $U_w^{+}(\omega) = \left[U_w(\omega) + i\phi_w(\omega)\right]/2$, finally the Fourier transform $W^{*}_{w_k}(\omega)$ of the minimum-phase wavelet $w^{*}_k(t)$ equivalent to $w_k(t)$ is computed by exponentiation of $U_w^{+}(\omega)$. The spiking deconvolution operator in the Fourier transform domain is:

$$F_{w_k}(\omega) = \frac{1}{W^{*}_{w_k}(\omega)} = \frac{1}{A^{*}_{w_k}(\omega)e^{i\phi^{*}_{w_k}(\omega)}} = A_f(\omega)e^{i\phi_f(\omega)} \tag{20}$$

where $A_f(\omega) = \dfrac{1}{\left[A^{*}_{w_k}(\omega) + \varepsilon\right]}$ and $\phi_f(\omega) = -\phi^{*}_{w_k}(\omega)$, with ε a small number in order to ensure that the filter is stable avoiding division by zero. This operation is called pre-whitening and is equivalent to adding a small amount of white noise to the signal. Under the assumption that earth reflectivity is a white process, the autocorrelation function of the recorded signal is a scaled version of the autocorrelation function of the source wavelet allowing estimation of a minimum-phase wavelet from the reconstructed signal $x^\wedge(t)$ in a similar manner. Earth reflectivity patterns, estimated by deconvolution of the reconstructed signal $x^\wedge(t)$ with the inverse of the equivalent minimum-phase Klauder wavelet, and that estimated from the reconstructed signal, shown in Fig. 5a, are compared with the reflectivity model in Fig. 5b. Results show a relatively good approximation with both methods.

2.3. Flattening and time slicing

The densely-spaced grid of high-resolution seismic reflection profiles collected in the Saros Gulf offered the opportunity to test pseudo-3D techniques and to image lateral changes of acoustic facies within the uppermost sedimentary sequence. After reconstructing the amplitudes of the seismic signal by inversion of the envelope, as described above, we removed any dipping structure from seismic data similarly to the method used for automatic residual static corrections with the compilation a "flattened" version of the seismic sections

by using a special function of the SeisPrho software. The flattened structures are obtained by time shifting the seafloor or any other reflector of interest within the sedimentary sequence, previously determined by detection algorithms or hand picking, to form new traces in which defined seismic event times are aligned at a horizontal reference level (0 ms in our case, Fig. 6). In this way, a new set of "flattened" SEGY files was created and subsequently sampled using the Time Slice function available in SeisPrho, which allows integration of squared seismic amplitudes (proportional to the seismic energy of reflections) within different time windows defined on the basis of local stratigraphy. This cumulative amplitude index, determined for each trace, has been considered as an estimate of seismic facies character and of the degree of lateral coherence of the selected reflector. In this case, we assumed that well layered beddings provide higher values of this coefficient than blind or chaotic deposits. We note that well-layered seismic facies, including alternating levels of finer and coarser grained deposits, give the maximum values of coherence, while "blind" or "transparent" facies, due to the presence of chaotic sediments, gas, or homogeneous levels without internal reflectors, correspond to minima of lateral coherence. However, this has been not considered a unique parameter for defining a seismic facies, and we used this proxy in conjunction with others (i.e. instantaneous attributes), and performed our interpretation after ground-truthing planview patterns on a map with seismic sections.

2.4. Maps compilation

Maps were compiled using the Generic Mapping Tool (GMT) software (Wessel and Smith, 1998). After filtering and editing the georeferenced points (bathymetry, reflectivity amplitude, etc), data were gridded using the nearest-neighbour algorithm of the GMT package.

3. Results

3.1. The seafloor

An example of seismic reflection profile crossing the NAF principal displacement zone in the Saros Gulf is shown in Fig. 6 (top), together with its flattened version (Fig. 6, bottom). The seismic profile M11_108 suggests a stratigraphy characterised by an erosional surface on which a > 10 m-thick sequence of well-layered deposits unconformably overlies. The seismic section also shows a main sub-vertical fault that offsets the entire sedimentary sequence up to the seafloor (Fig. 6), representing the trace of the NAF principal displacement zone in this area. Other minor details include the presence of gas pockets, which hamper penetration of the seismic signal and reflections in the water column probably due to shoals of fish (Fig. 6).

The first information that can be gathered by the densely spaced set of collected data (Fig. 7a) is bathymetry. The bathymetric contour map displayed in Fig. 7b was obtained by gridding the *xyz* output of the Bottom Detection algorithm included in SeisPrho, subsequently converting the two-way travel times (TWT) into depths assuming a constant sound velocity of 1500 m/s in the water column. The map shows a narrow valley, extending and deepening towards WSW, from water depths between 40 to 100 m. This depth interval, together with the low topographic gradients, allow us to assume the close-spaced density of the seismic lines a 3D representation of the seafloor and of the shallow sub-seafloor. The bathymetric grid obtained, enabled us to compile a slope map of the seafloor (Fig. 7c).
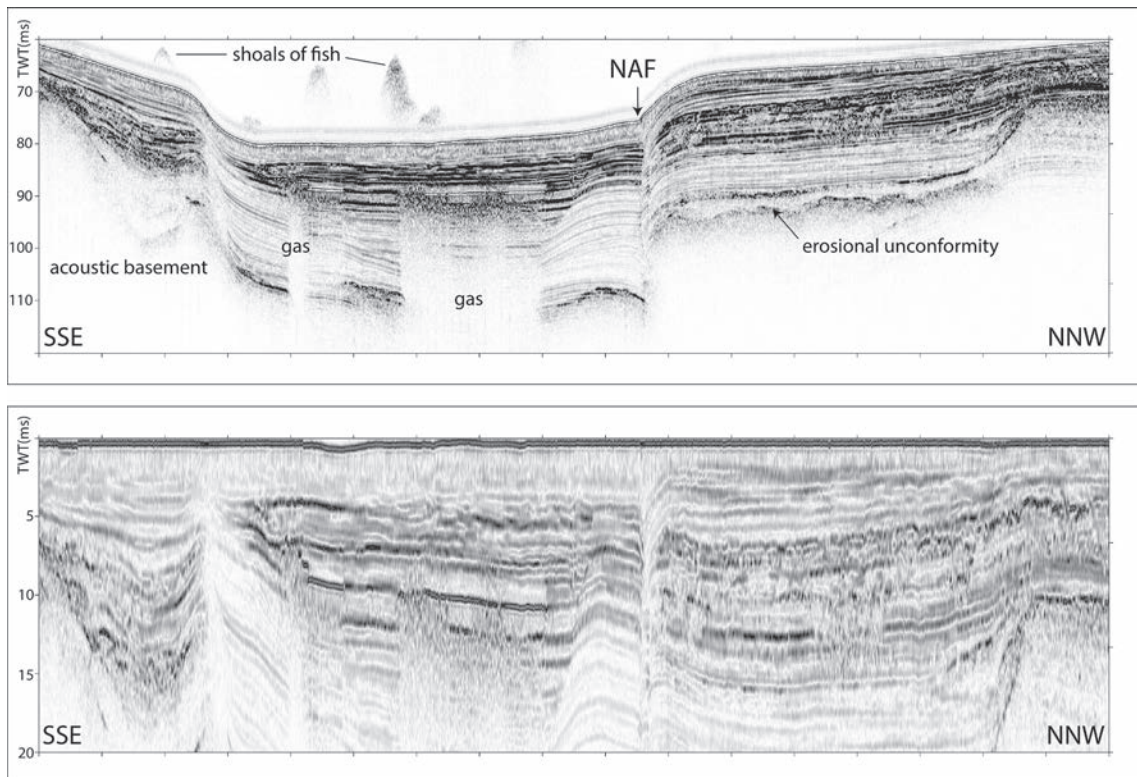
Fig. 6 - Top: seismic reflection profile M11_108 crossing NW-SE the study area (location in Fig. 7a). Bottom: flattened version of the same profile.

This representation of the data highlights a sharp, distinct discontinuity at the centre of the valley, which corresponds to the NAF principal displacement zone. We note how the fault trace is sharp and characterised by a linear geometry, as well as a sequence of oversteps towards the north, which in the left-lateral strike-slip regime produces small, flat ponds filled with sediments. The last map in Fig. 7d shows the distribution of instantaneous amplitudes (reflection strength) obtained point by point as the maximum amplitude value of signal envelope (see the Methods section) at the seafloor reflector. These data provide information on the reflectivity of the seafloor and represent the seismic facies character of surficial sediment distribution. In fact, although propagation and scattering of high frequency acoustic waves at or near the sea bottom are controlled by a number of factors, including biological, geological, biogeochemical, and hydrodynamic processes operating at the benthic boundary layer (Richardson and Briggs, 1996), experimental measurements suggest that the most important geotechnical property related to acoustic attenuation is the mean grain size of the insonified sediment (Shumway, 1960; Gasperini, 2005). Quantitative analysis of reflectivity is feasible only for the seafloor reflector, assuming a homogeneous water column. In most cases, this is a reasonable assumption except when an obstacle (plants, fishes, etc) is located between the seismic source and the seafloor (Fig. 6). This measure could be used for seafloor classification, and to gather information on ongoing processes that actually affect sediment distribution. However, in order to refer reflectivity to a specific seafloor characteristic, a validation procedure is required, based on analysis of sediment samples.

Fig. 7d suggests that the water depth is the main parameter controlling reflectivity, because higher reflectivity values (red colour) are found in the shallower area. Although in this case study, ground-truthing samples are not available and our analysis is only qualitative, we could assume that grain size is the primary controlling factor for reflectivity (higher reflectivity = larger average grain size), and thus there is a gradient of this parameter from the coast to the deeper levels. This in turn would imply hydraulic sorting of the sediments, probably due to turbidite or hyperpicnal flows. The lowest values of reflectivity are observed in the rhomb-shaped depressions aligned along the southern flank of the NAF principal displacement zone (Fig. 7d, blue pattern). These values indicate that most of the fine grained deposits are trapped within those ponds.

3.2. Pseudo 3D images of the subsurface

Flattening of all seismic reflection lines was performed to obtain a volume of insonified sub-seafloor after application of spherical divergence correction to the seismic trace amplitudes. This volume was time sliced to obtain a 2D representation of reflectivity patterns at discrete time levels, to visualise lateral variations in sediment properties and deformation, and to infer geological properties. Fig. 8 displays a sequence of time levels obtained by sampling and gridding amplitude values within the seismic profile network. Interpretation of single geological features is beyond the scope of this study, since it also implies a stratigraphic analysis of sediment cores not available to the present work. However, we note that maps of cumulative amplitude index distribution at different levels highlight
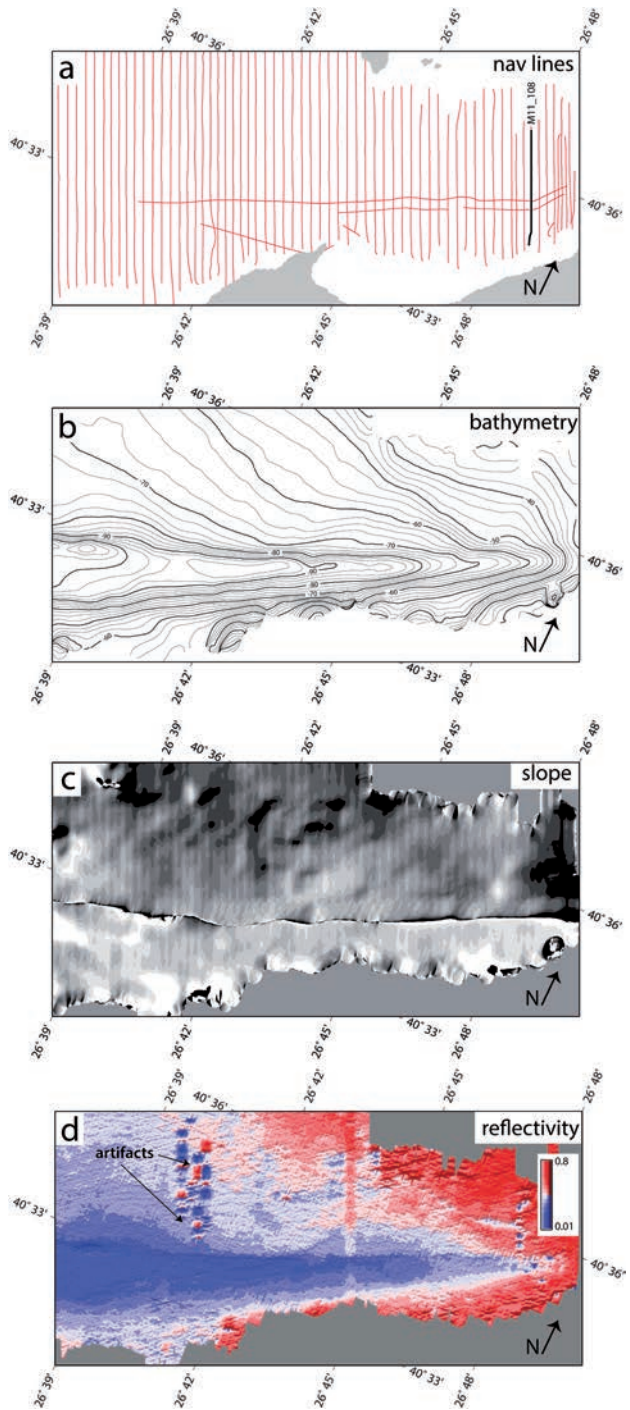

Fig. 7 - a) Navigation lines of the seismic reflection profiles used for this work. Position of Line M11_108 shown in Fig. 6 is indicated. b) Bathymetric contour map (isobaths each 2.5 m) derived by picking the seafloor reflector. c) Slope map compiled using bathymetric data. d) Reflectivity map. Projection is Oblique Mercator, Datum, WGS84.
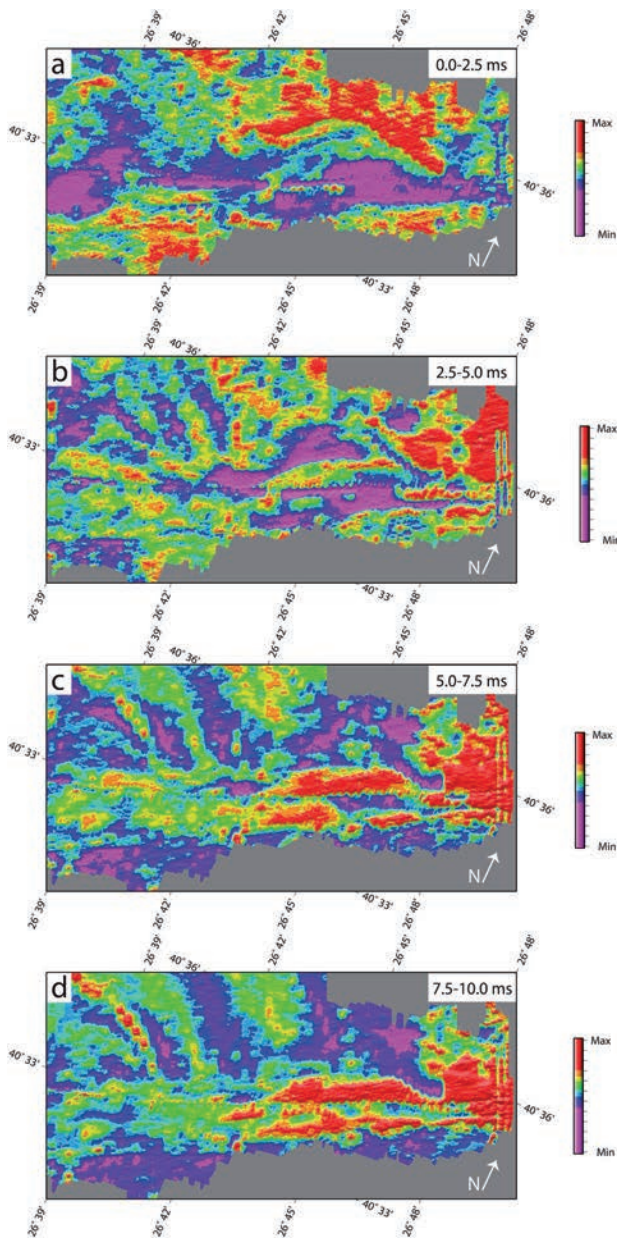
Fig. 8 - Shaded-relief colour-coded representation of integrated, normalised reflectivity (see text) at different levels in the stratigraphic column: a) between 0 and 2.5 ms; b) 2.5-5.0 ms; c) 5.0-7.5 ms; d) 7.5-10.0 ms. Projection is Oblique Mercator, Datum, WGS84.

sedimentary and structural features that would help geological interpretation of seismic sections. The amplitude index grid displayed in Fig. 8a includes the shallowest stratigraphic interval with the seafloor and the first 2.5 ms TWT interval of sub-seafloor. We note that the deformation zone along the NAF appears more complex relative to that shown by the morpho-bathymetric map of Fig. 7c. In fact, we can observe other rectilinear lineaments oriented NE-SW, subparallel to the NAF trace, which displace sedimentary bodies characterised by different acoustic properties. An arcuate feature delineated by high values of the amplitude index (red colours) is also observed just north of the NAF principal displacement zone. This feature disappears at depth as shown in the deeper grids including the amplitude index evaluated in TWT intervals greater than 2.5 ms (Figs. 8b, 8c, and 8d).

The time slice displayed in Fig. 8d is the deepest for the study area (7.5 - 10.0 ms) and shows a complex deformation pattern along the NAF trace, with the presence of displaced sedimentary bodies elongated in the SW-NE direction and "stretched" by the strike-slip deformation along the main fault. Other interesting features are represented by a series of arcuate morphologies sub parallel to the contour lines. The most prominent of these features is found close to the western edge of the study area. Although direct sampling and stratigraphic studies are needed, we may speculate that such bodies, characterised by high seismic amplitudes represent coarse-grained deposits accumulated during the complex sea level transgression following the Last Glacial Maximum, since they are stratigraphically located immediately above the erosional surface marking subaerial exposure (Fig. 6a).

The availability of such maps, while not allowing stratigraphic reconstructions, may represent an effective tool for planning further studies based on sediment sampling.

4. Conclusions

We presented algorithms and methods to compile pseudo-3D maps of the subsurface based on high resolution seismic reflection profiles collected using CHIRP-sonar marine sources. Results enabled us to describe (although in absence of direct sampling and stratigraphic data fundamental to geological interpretation) the distribution of seismic facies in the Saros Gulf, a shallow-water marine environment in the NE Aegean Sea, along the NAF principal displacement zone. The time-slice seismic amplitude images of different stratigraphic levels, obtained using innovative techniques are suggestive of a complex pattern of sea level changes and tectonic deformation. Such images, integrated by direct samplings of the sediment and stratigraphic analysis, could represent an interesting tool to study geometry and lateral variability of the geological features.

REFERENCES

Claerbout J.F.; 1985: *Fundamentals in geophysical data processing*. Blackwell Scientific Publications, Palo Alto, CA, USA, 280 pp.

Dal Forno G. and Gasperini L.; 2008: *ChirCor: a new tool for generating chirp-sonar seismograms*. Comput. Geosci., 34, 103-114.

Gasperini L.; 2005: *Extremely shallow-water morphobathymetric surveys: the Valle Fattibello (Comacchio, Italy) test case*. Mar. Geophys. Res., 26, 97-107.

Gasperini L. and Stanghellini G.; 2009: *SeisPrho: an interactive computer program for processing and interpretation of high-resolution seismic reflection profiles*. Comput. Geosci., 35, 1497-1507.

Gasperini L., Polonia A., Çağatay M.N., Bortoluzzi G. and Ferrante V.; 2011a: *Geological slip rates along the North Anatolian Fault in the Marmara region*. Tectonics, 30, TC6001, doi: 10.1029/2011TC002906.

Gasperini L., Ülgen U.B., Angeletti L., Bortoluzzi G., Dalpasso E., Del Bianco F., Acar D., Aksoy M.E., Özmaral A., Can A.Z., Şimşek B., Öcal F., Elbek S., Uluğ A., Maddalena M., Ricchi A., Poliseno A., Tudino T., Raspagliosi M. and Urzi F.; 2011b: *MARM11: marine geological study of the North Anatolian Fault beneath the Saros Gulf (N. Aegean Sea), R/V Urania cruise report (2011/09/23 - 2011/10/10)*. Ismar-CNR, Bologna, Italy, Technical Reports, 55 pp., <www.ismar.cnr.it/products/reports-campagne>.

Gasperini L., Marzocchi A., Mazza S., Miele R., Meli M., Najjar H., Michetti A.M. and Polonia A.; 2020: *Morphotectonics and late Quaternary seismic stratigraphy of Lake Garda (Northern Italy)*. Geomorphol., 371, 107427, doi: 10.1016/j.geomorph.2020.107427.

Gutzwiller O.; 1921: *Beitragezur zur geologie der umgebung von Merfete am Marmara-Meer*. Thesis, University of Basel, Basel, Switzerland, 36 pp.

Harris F.J.; 1978: *On the use of windows for harmonic analysis with discrete Fourier transform*. Proc. IEEE, 66, 51-83, doi: 10.1109/PROC.1978.10837.

Hayes M.H., Lim J.S. and Oppenheim A.V.; 1980: *Signal reconstruction from phase or magnitude*. IEEE Trans. Acoust. Speech Signal Process., ASSP-28, 672-680.

Kumaresan R. and Rao A.; 1999: *Model-based approach to envelope and positive instantaneous frequency estimation of signals with speech applications*. J. Acoust. Soc. Am., 105, 1912-1924, doi: 10.1121/1.426727.

Ligi M., Bortoluzzi G., Giglio F., Del Bianco F., Ferrante V., Gasperini L. and Ravaioli M.; 2018: *Shallow water acoustic techniques to investigate transitional environments: a case study over Boka Kotorska bay*. Meas., 126, 382-391.

Oppenheim A.V. and Schafer R.W.; 2010: *Discrete-time signal processing, 3rd ed.* Pearson Higher Education Inc., Upper Saddle River, NJ, USA, 1136 pp.

Richardson M.D. and Briggs K.B.; 1996: *In situ and laboratory geoacoustic measurements in soft mud and hard-packed sand sediments: implications for high-frequency acoustic propagation and scattering*. Geo-Mar. Lett., 16, 196-203.

Schock S.G., LeBlanc L.R. and Mayer L.A.; 1989: *Chirp subbottom profiler for quantitative sediment analysis*. Geophys., 54, 445-450.

Shumway G.; 1960: *Sound speed and adsorption studies of marine sediments by resonance method - part 1*. Geophys., 25, 451-467.

Stanghellini G., Del Bianco F. and Gasperini L.; 2020: *OpenSWAP, an open architecture, low cost class of autonomous surface vehicles for geophysical surveys in the shallow water environment. Remote Sens., 12*, 2575.

Voelcker H.B.; 1966: *Toward a unified theory of modulation part I: phase-envelope relationships*. Proc. IEEE, 54, 340-353.

Yilmaz Ö.; 2001: *Seismic data analysis: processing, inversion, and interpretation of seismic data*. In: Doherty S.M. (ed), Investigation in Geophysics, Society of Exploration Geophysicists Book, Tulsa, OK, USA, pp. 2023-2027.

Wessel P. and Smith W.H.; 1998: *New, improved version of generic mapping tools released*. Eos, Trans. AGU, 79, 579, doi: 10.1029/98EO00426.

Corresponding author: Luca Gasperini
                            Istituto di Scienze Marine, Consiglio Nazionale delle Ricerche (ISMAR-CNR), Sezione di Bologna
                            Via Gobetti 101, 40129 Bologna, Italy
                            Phone: +39 051 6398901; e-mail: luca.gasperini@ismar.cnr.it